Journal of Materials Chemistry A

Accepted Manuscript

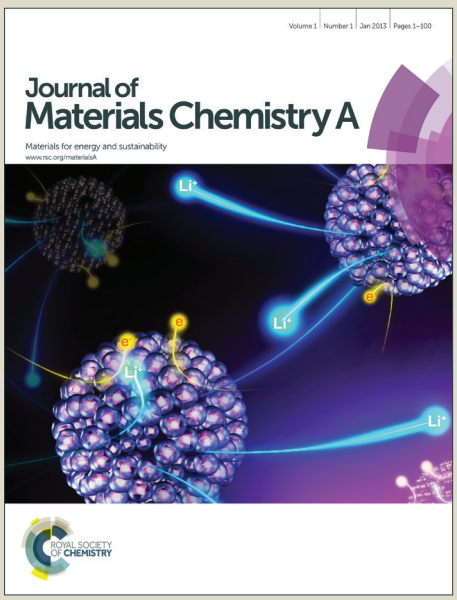

This is an *Accepted Manuscript*, which has been through the Royal Society of Chemistry peer review process and has been accepted for publication.

Accepted Manuscripts are published online shortly after acceptance, before technical editing, formatting and proof reading. Using this free service, authors can make their results available to the community, in citable form, before we publish the edited article. We will replace this *Accepted Manuscript* with the edited and formatted *Advance Article* as soon as it is available.

You can find more information about *Accepted Manuscripts* in the Information for Authors.

Please note that technical editing may introduce minor changes to the text and/or graphics, which may alter content. The journal's standard Terms & Conditions and the Ethical guidelines still apply. In no event shall the Royal Society of Chemistry be held responsible for any errors or omissions in this *Accepted Manuscript* or any consequences arising from the use of any information it contains.

ROYAL SOCIETY OF CHEMISTRY

www.rsc.org/materialsA

Cite this: DOI: 10.1039/c0xx00000x

www.rsc.org/xxxxxx

PAPER

High Electrochemical performance in Asymmetric Supercapacitors using MWCNTs/Nickel Sulfide Composite and Graphene Nanoplatelets as Electrodes

Arvinder Singh,[1] Alexander J. Roberts, *[2] Robert C. T. Slade[2] and Amreesh Chandra*[1]

Received (in XXX, XXX) XthXXXXXXXXX 20XX, Accepted Xth XXXXXXXXX 20XX
DOI: 10.1039/b000000x

The electrochemical performance of asymmetric supercapacitors (ASCs) using MWCNTs/NiS and graphene nanoplatelets as positive and negative electrode, respectively, are reported. Nickel sulfide nanoparticles can be decorated on multiwall carbon nanotubes using a hydrothermal synthesis process, with graphene nanoplatelets obtained via a chemical route. The fabricated ACSs were operated over a potential window of 1.4 V with a specific capacitance of 181 F g^{-1} observed at 1 A g^{-1}. The ASCs were cycled at 2 A g^{-1} showing 92% retention of initial capacitance after 1000 cycles.

.

1. Introduction

Recent global research in exploitation of novel electrochemical energy storage devices (ESDs) has focused on numerous applications ranging from consumer electronics to hybrid vehicles.[1] One such ESD attracting much attention is the electrochemical supercapacitor (SC), with intrinsic properties of high power density, long cyclic life and a wide operating temperature range.[2] The energy density (E) of SC is still low in comparison to batteries and this limits its full utilization over a range of applications. Since increasing E is directly linked to the increase in capacitance, modern day research is focused on the development of nanostructured electrode materials (primarily based on various forms of carbon such as graphene oxide, graphene, MWCNTs etc.) with tailored surface area and porosity.[3-5] Recently, with the introduction of pseudocapacitive/ redox materials (transition metal oxides, conducting polymers, metal sulfides) in SCs, large increase in specific capacitance have been achieved in comparison to the carbon materials.[6-7] E is also directly proportional to the square of the electrical potential window of operation. The use of non-aqueous electrolytes allows a much larger potential window to their aqueous counterparts but brings detrimental effects on device performance due to low ionic conductivity and high viscosity.[8-9] Aqueous electrolytes are commonly used in both asymmetric supercapacitors containing one carbon based and one pseudocapacative electrode and in carbon/carbon electrode systems.[10-11] Such electrolytes are limited thermodynamically to a potential window of approximately 1.2 V. This value can be extended by utilization of the overpotentials encountered during the use of some metal oxide materials or by manipulation of the anodic and cathodic potentials attained through careful unbalancing of electrodes during the fabrication of devices.[12]

Amongst the forms of carbonaceous materials, multiwall carbon nanotubes (MWCNTs) have been used extensively in SCs due to their high electrical conductivity, chemical stability and tuneable surface area. In the case of metal sulfides, NiS has been identified as an excellent pseudocapacitive (redox) material because of its high conductivity and redox properties at room temperature. Nickel sulfide is found in various complex phases and has wide range of applications.[13-15] There are several reports investigating individual electrochemical performance of MWCNTs and NiS in SCs where NiS is used in the positive electrodes.[16-20] Of the carbon-based materials under consideration for the negative electrode in ASCs, exfoliated graphene nanoplatelets (GNPs) have attained prominence due to their high surface area, electronic conductivity and chemical stability at negative potentials. Several reports demonstrating successful operation of SCs using GNPs and/or graphene as negative electrode materials within a wide operating cell voltage window (0 to 1.4-1.8 V) have recently been published.[21-22]

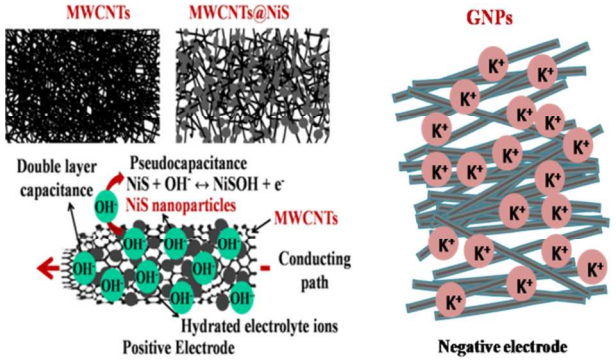

Fig. 1 Schematic showing role of each component in electrodes

Journal of Materials Chemistry A Accepted Manuscript

In the current work, hydrothermally synthesized MWCNTs/Nickel sulfide (MWNS) composite and graphene nanoplatelets were used as electrode materials for the positive and negative electrodes, respectively. The role of each component in both the electrode materials is depicted in Fig. 1. The ASCs were fabricated with KOH (aq, 6 mol dm^{-3}) electrolyte which can be operated up to 1.4 V. A maximum specific capacitance of 181 F g^{-1} is observed at a specific current of 1 A g^{-1}, when both the electrodes are properly charge balanced. Furthermore, the ACS shows ~92% retention of the initial capacitance (~165 F g^{-1}) after 1000 cycles operation at a specific current of 2 A g^{-1}. In comparison to pure NiS, MWCNTs and GNPs, our ASCs have shown promising electrochemical results and have potential for application in a range of technologies.

2. Experimental

2.1 Materials synthesis and characterization

Nickel (II) acetate tetrahydrate and thiourea were purchased from Sigma Aldrich (U. K.). Multiwall carbon nanotubes (MWCNTs) (ID 3-5 nm; OD 20-25 nm; length 20 μm and purity 95%) were purchased from Nanocyl (Belgium). Sulfuric acid (98%), hydrogen peroxide solution GR (30%) and potassium permanganate (98.5%) were purchased from Merck Specialities Pvt. Ltd. (India). Graphite fine powder (particle size 50 μm, purity 99%) and glucose were purchased from Loba Chemie Pvt. Ltd. (India). All chemicals were used without further purification.

MWCNTs were surface functionalized in nitric acid (69 wt%) solution for 24 h. For the synthesis of composite, nickel acetate (2.74 g, 36.7 mmol) was dissolved in 300 cm^3 de-ionized (DI) water and stirred at room temperature for 0.5 h. 4 g acid-treated MWCNTs were added and the resulting suspension stirred overnight at room temperature. 9.00 g thiourea (394 mmol) was then added and transferred to 600 cm^3 capacity Hastelloy steel autoclave (Parr) and heated to 140 ºC for 4 h. The resultant black solid was filtered and washed several times with DI water and, finally, vacuum dried at 60 °C for 12 h. NiS nanoparticles were synthesized by the same method in absence of MWCNTs. For the graphene synthesis, first, graphite oxide (GO) was synthesized by Hummer's method.[23] In brief, a mixture of 3.00 g graphite powder, 1.50 g $NaNO_3$ and 69 mL concentrated H_2SO_4 was stirred for 10 minutes at 0 ºC. Then, 9.00 g $KMnO_4$ was added tardily to maintain the reaction temperature below 20 ºC. After that, mixture was stirred at 35 ºC for 30 minutes. Then, solution was diluted with 140 mL DI water which increased the temperature of the solution to 98 ºC. The solution was maintained at this temperature for 15 minutes using external heating. The solution was further diluted with 420 mL DI water and finally, 3 mL 30% H_2O_2 was added. Then, solution was cooled to room temperature and GO was collected by centrifugation, washing several times with DI water and vacuum drying at 50 ºC for 24 h. Graphene nanoplatelets were synthesized by reducing GO using glucose as a reducing agent.[24] In brief, GO (0.2 mg mL^{-1}) was dispersed homogeneously in 50 mL DI water using ultrasonication. After that, about 80 mg glucose was added and whole solution was stirred for 2 h. Subsequently, 0.4 mL ammonia solution was added and solution was stirred further for 2 h at 95 ºC. The final black product was filtered, washed with DI water several times and dried at room temperature in a vacuum oven for 48 h.

The X-ray powder diffraction data were collected in 2θ range 10-90° on PanAnalytical XPert diffractometer with CuK_α incident radiation. Field emission scanning electron microscopy (FESEM) and transmission electron microscopy (TEM) measurements were performed using SEM CARL ZEISS SUPRA 40 and TEMFEI-TECHNAI G220S-Twin operated at 200 kV. X-ray photoelectron spectroscopy (XPS) was carried out using the PHI 5000VERSAProbe II X-ray photoelectron spectrometer with AlK_α as incident photon energy. A Keithley 2612B source-meter was used to perform four-probe resistivity measurements. The Brunauer- Emmett-Teller (BET) surface area and porosity were measured by analysing adsorption-desorption isotherms obtained using Micromeritics Gemini V Model 2365 and Gemini VII Model 2390t. Thermogravimetric analysis (TGA) was carried out in O_2 environment at 10 °C min^{-1} from room temperature to 800 °C using NETZSCH STA 409 PC/PG thermal analyzer. Raman measurements were performed on powder sample with the help of Micro-Raman spectrometer LABRAM HR from Horiba Jobin Yvon with 488 nm excitation wavelength of an Ar-ion laser.

2.2 Electrode preparation and electrochemical measurements

Both three-electrode and two-electrode systems were used, in order to investigate electrochemical performance of single electrode and cell assembly, respectively. Activated carbon was used as counter electrode and Ag/AgCl (sat. KCl) was used as reference electrode. The working electrode was fabricated with 95 mass% of active materials and 5 mass% PVDF which were well dispersed in acetone using ultrasonication and stirred at 80 ºC to form a homogeneous ink. The electrodes were drop-casted with a mass loading ranging from 0.2 to 0.4 mg on stainless steel foil (~25 μm thick) followed by oven drying at 100 ºC. Counter electrodes were fabricated using 80% activated carbon, 10% graphite and 10% polyvinylidene fluoride (PVDF). Full electrochemical characterization was carried out using cyclic voltammetry (CV), galvanostatic charge-discharge, and electrochemical impedance spectroscopy (EIS) using a Metrohm Autolab (Galvanostat/Potentiostat).

3. Results and discussion

Phase and crystallinity of the electrode materials have significant influence on SC performance. In order to determine phase and crystallinity, synthesized materials were analysed using X-ray powder diffraction (XRD). The typical XRD patterns of MWCNTs and MWNS composite are shown in Fig. 2(a). Diffraction peaks at 2θ ~25.4° and 42.6° for MWCNTs are associated with (002) and (100) planes, respectively, according to the JCPDS file no. 250284. The shift towards lower 2θ of the (002) peak in MWCNTs in comparison to graphite (26.5°) can be attributed to an increase in spacing between the sp^2 hybridized layers. The remaining diffraction peaks observed in MWCNTs at 2θ~53.1°, 63.9°, 77.9° and 81.6° correspond to (004), (103), (110) and (112) planes. Both the characteristic peaks ((002) and

Journal of Materials Chemistry A Accepted Manuscript

This journal is © The Royal Society of Chemistry [year]

(100)) re-emerged at nearly the same 2θ value in the case of the MWNS composite. New peaks in the MWNS composite could be indexed to the rhombohedral β-phase of NiS according to JCPDS file no. 120041. The average crystallite size of the NiS nanoparticles in MWNS composite is calculated using Scherrer equation:

$$D = 0.89\lambda/\beta\cos\theta$$

where λ is the used wavelength, β is the full width half maxima and θ is the diffraction angle for the most intense peak (here (110) for NiS nanoparticles in MWNS composite). The average crystallite size is found to be 20.8 nm which is smaller than that observed in TEM images, suggesting self-assembling of NiS nanoparticles in larger crystallite. The XRD pattern of NiS nanoparticles is also given in supplementary information (see ESI Fig. S1(a)).

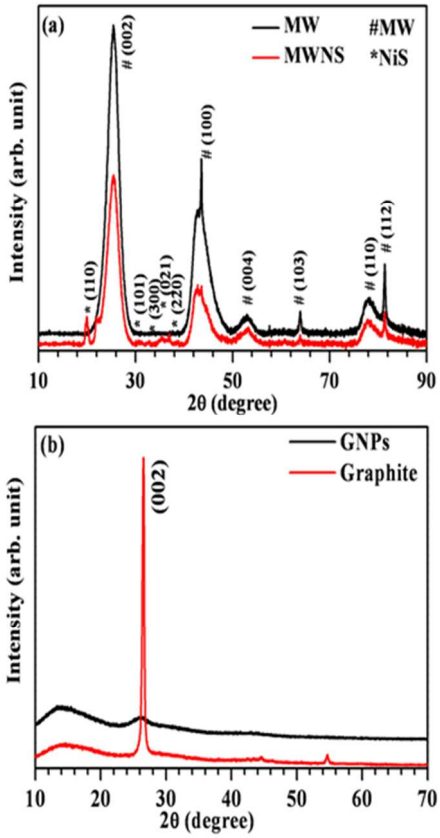

Fig. 2 XRD patterns for (a) MWCNTs (MW) and MWNS composite and (b) graphite and GNPs

Fig. 2(b) shows the XRD pattern for graphite and GNPs. In the case of GNPs, the oxidation, exfoliation and subsequent reduction results in a broadening of the (002) peak.[24]

The morphology of the electrode material has significant effect on the performance of SCs as it governs the surface area, porosity and accessibility of electrolyte into the electrode surface. Fig. 3(a) shows an FESEM micrograph of MWCNTs and Fig. 3(b-c) shows the FESEM images for MWNS composite collected at

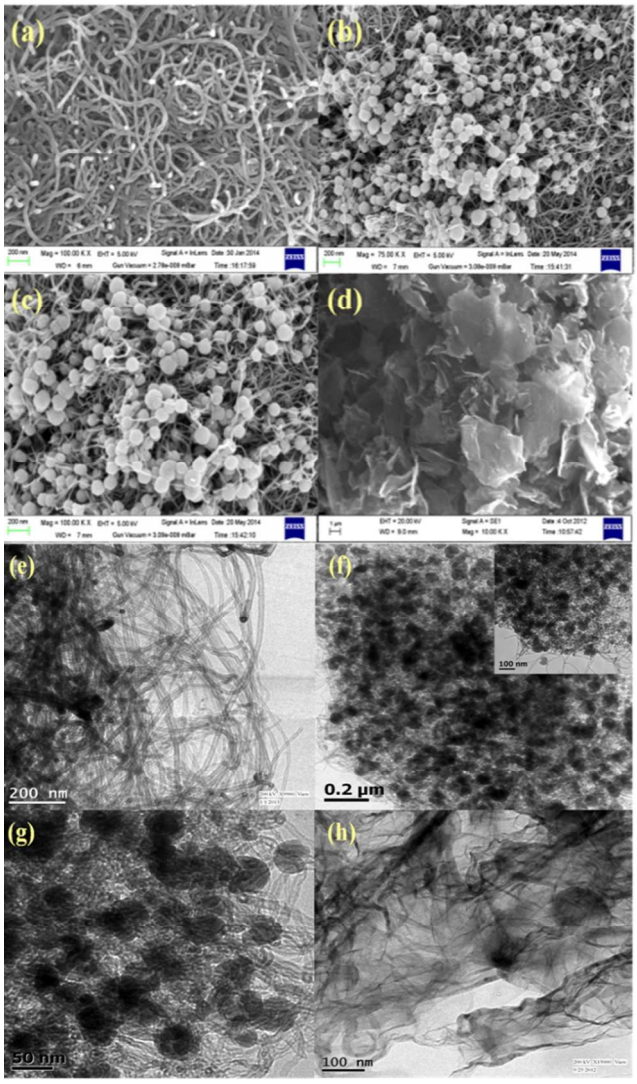

Fig. 3 FESEM micrographs of (a) MWCNTs (b-c) MWNS (d) GNPs and TEM micrographs of (e) MWCNTs (f-g) MWNS (h) GNPs. An inset to (f) shows a TEM micrograph of MWNS at higher magnification.

different magnification. Large micron sized bundles of entangled MWCNTs were observed in both the cases while the presence of NiS nanoparticles is apparent in the case of MWNS composite. A SEM micrograph for NiS is given in Fig. S1(b) (see ESI). The growth of NiS nanoparticles on MWCNTs surface is confirmed by the TEM micrographs..

Fig. 3(e) depicts the TEM micrograph of entangled MWCNTs. The dark and light portions observed in the sample depict the surface and core structure of CNTs. TEM micrographs of MWNS composite taken at different portions of the sample are shown in Fig. 3(f-g). The TEM micrographs confirm that the surface of MWCNTs have been decorated with NiS nanoparticles of a wide particle size distribution. Fig. 3(d) shows the SEM micrograph of GNPs which possesses partially overlapped flake-like graphene sheets. Further, the flake-like morphology of GNPs is confirmed by the TEM micrograph, where wrinkles could be assigned to defects, remaining functional groups and/or partial overlapping of

Journal of Materials Chemistry A Accepted Manuscript

GNPs as depicted in Fig. 3(h).

X-ray photoelectron spectroscopy (XPS) was used for investigating surface functionality of GNPs, and the chemical composition and oxidation state of nickel in the composite system. The XPS core level spectrum of C 1s in MWNS is depicted in Fig. 4(a). A typical graphitic C 1s peak, due to MWCNTs, was clearly observed at ~284.6 eV while two peaks in the shoulder of this C 1s; peak appearing at ~286.9 and ~289.6 eV respectively, are due to residual C-OH and -COOH groups on the MWCNTs surface. The core level spectra of S 2p and Ni 2p for MWNS composite are depicted in Fig. 4(b-c), respectively. These spectra were fitted using an asymmetric Gaussian-Lorentzian profile function with a Shirley background.

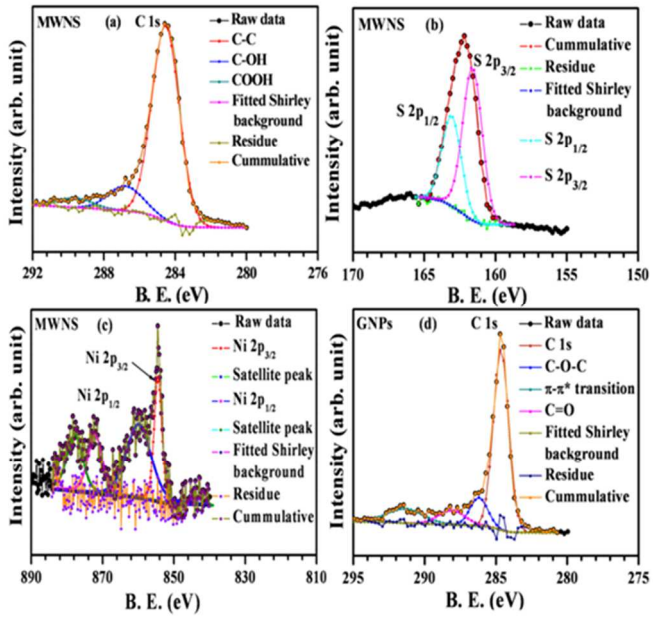

Fig. 4 XPS core level spectra of (a) C 1s (b) S 2p (c) Ni 2p in MWNS and (d) C 1s in GNPs.

The observed S 2p spectrum shows a doublet near the binding energy of ~162.1 eV. The two components are associated with S $2p_{3/2}$ and S $2p_{1/2}$ states and appeared at ~161.9 and ~163.1 eV, respectively. This doublet confirms the formation of nickel monosulfide nanoparticles. There was no apparent signature of any additional Ni_3S_2 phase (binding energies of S 2p core level in Ni_3S_2 are reported between ~162.4-162.8 eV).[25] Further, in the case of Ni 2p spectra, the main Ni $2p_{3/2}$ and Ni $2p_{1/2}$ peaks appear at ~854.4 and ~871.9 eV, respectively, each having one satellite peak. These results are consistent with the previous literature,[25] showing successful formation of MWNS composite. The XPS analysis shows the atomic composition of MWNS composite C=86.4, Ni=5.2, S=5.2 and O=3.2%. The small amount of oxygen is due to residual gases present in the analytical chamber and/or remaining functionality on MWCNTs surface.

Fig. 4(d) shows the characteristic C 1s spectrum of GNPs (at ~284.6 eV) comprising of three de-convoluted components: one at ~286.2 eV is due to the epoxide (C-O-C) group while the second at ~288.2 eV originates from >C=O (carbonyl) group. The origin of the third component appearing at ~291.5 eV, also known as a shake-up satellite peak, lies in π-π* transition of sp^2 carbons i.e. refurbishment of aromaticity after reduction to GNPs.[26] These results clearly show reduction of graphite oxide to GNPs.

To determine the accurate weight percentage of NiS nanoparticles in the MWNS composites, thermogravimetric analysis (TGA) was performed for both functionalized MW and as-prepared MWNS composite (see ESI Fig. S2). The weight loss below 100ºC in the MWNS composite and MW is attributed to removal of the adsorbed water. It can be seen that the annealing/decomposition of the functionalized MW results in further weight loss in both the samples (500-600 °C). The weight percentage of NiS nanoparticles in the MWNS composite was found to be ~33 wt%, when compared with the residual weight percentage of the functionalized MWCNTs (10.0 wt%).

Raman spectra were also collected for the GNPs, MW and MWNS samples. These are shown in Fig. 5(a-b). Raman spectrum of GNPs (Fig. 5(a)) exhibits two characteristic D and G-bands appearing at ~1355 and ~1576 cm^{-1}. The origin of the D band lies in the disorder present in the sp^2 carbon atoms, edges or other defects whereas the G band originates because of the scattering from the in-plane sp^2 carbon atoms. Other characteristic 2D peak arises at 2698 cm^{-1} with an intensity ratio of I_G/I_{2D} = 1.21 for the GNPs.

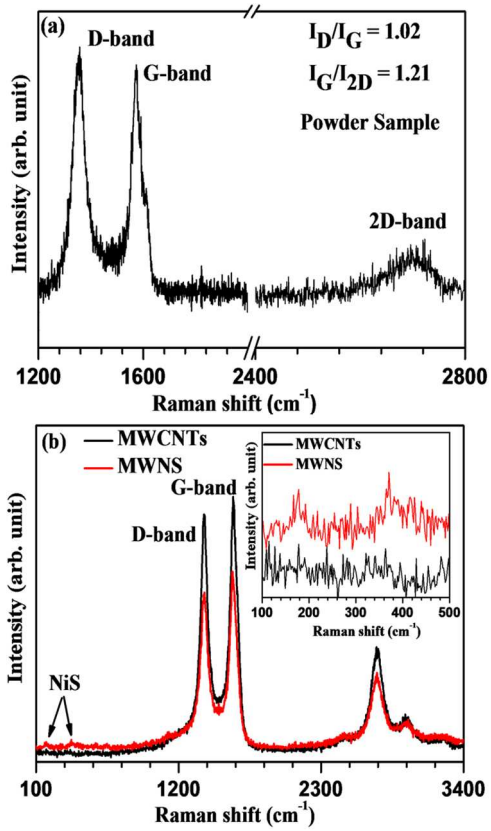

Fig. 5 Raman spectra observed for (a) GNPs and (b) MW and MWNS composite

MW also displays two characteristics graphitic D and G-bands (depicted in Fig. 5(b)) and one overtone G' band appearing at 1399, 1620 and 2734 cm^{-1}, respectively. The G-band arises due to

Journal of Materials Chemistry A Accepted Manuscript

This journal is © The Royal Society of Chemistry [year]

the in-plane vibrations of C-C carbons whereas the later originates due to the disorder in the carbon networks. In the case of MWNS composite, two extra Raman modes are observed at ~168 and ~369 cm^{-1}, which are in well agreement with the previously reported Raman modes for β-NiS samples.[27] However, all the vibration modes for NiS were not observed which may be associated with the effect of quantum confinement on the vibrational modes in the NiS nanoparticles. [28-29]

Brunauer-Emmett-Teller (BET) surface area and porosity were estimated for GNPs and MWNS composite by analysing the adsorption-desorption isotherms (see ESI Fig. S3). These isotherms observed for the MWNS composite and GNPs represent type IV isotherm with H3 hysteresis. This suggests presence of mesopores in the GNPs and MWNS composite with narrow short necks and slit-shaped pores. An inset to Fig. S3 shows the pore size distribution. It can be seen that most of the pores lies in the mesopores region. The BET surface area for the GNPs and MWNS composite was found to be 13.9 and 168.4 $m^2 g^{-1}$, respectively.

Further, electrical conductivity of the functionalized MWCNTs, MWNS, NiS and GNPs was investigated using the four probe resistivity measurements on compact disk shaped samples (pellets). The following equations were used to calculate conductivity from I-V curves (see ESI Fig. S4):

$$\text{Resistivity } (\rho, \text{ohm.cm}) = (\pi t/\ln 2)*(V/I)$$

and

$$\text{Conductivity } (\sigma, \text{S cm}^{-1}) = 1/\rho$$

where t = thickness of the sample, V = measured voltage and I = current. Conductivity (σ) of MWCNTs, MWNS, NiS and GNPs were found to be ~5.2, 4.8, 4.5 and 0.3 S cm^{-1}, respectively. The MWNS composite showed reduced electrical conductivity in comparison to functionalized MWCNTs. This can be attributed to the presence of NiS nanoparticles and defect formation in the MWCNTs structure. However, even after decoration, the MWNS composite possesses good electrical conductivity due to the preserved long chain characteristics of inner CNTs present in the MWNS matrix (as is apparent in TEM images).

In order to correctly balance the electrodes in full cell test supercapacitors, cyclic voltammetry (CV) experiments were carried out over a wide range of scan rates in a three electrode system. Quasi-rectangular CV traces were observed at each scan rate with small hump for GNPs as shown in Fig. 6(a); this confirmed presence of electric double layer capacitance as well as pseudocapacitance (could be originated due to residual functional group), with good reversible diffusion through the electrode material. The specific capacitance of the working electrode material was determined according to the following equation:

$$C \text{ (F g}^{-1}) = (1/mVs) \int idv$$

where *m* is the mass of the active material (~0.2 mg in the present study), *V* is the total voltage range scanned (0.8 V; -0.1 to -0.9 V), *s* denotes scan rate, and $(1/s)\int idv$ is the total charge accumulated inside the electrode material. The maximum specific capacitance observed at 20 mV s^{-1} scan rate was ~144 F g^{-1}.

CV measurements were also carried out on MW, NiS and MWNS composite at 20 mV s^{-1} which are given in Fig. S5 (see ESI). MW exhibited nearly rectangular shape CV curve while NiS and MWNS both possesses redox peaks due to pseudocapacitance originated by redox reaction. It can be seen that MWNS composite shows higher charge storage capacity in comparison to pure MW and NiS. This is due to improved conductivity and high surface area of the MWNS composite (168.4 $m^2 g^{-1}$) which facilitates deeper penetration of electrolyte ions into electrode materials and thus gives higher capacitance in comparison to individual components (positive synergic effect between NiS nanoparticles and MW). Further, CV curves observed for the MWNS composite in the positive potential range (-0.1 to 0.5 V) over a range of scan rates are shown in Fig. 6(b). A pair of pronounced redox peaks were observed in the CV curves which could be assigned to the redox process associated with NiS charge/discharge:

$$NiS + OH^- = NiSOH + e^-$$

It is noteworthy that, for MWNS, a higher current was observed in comparison to GNPs. This can be attributed to the additional pseudocapacitance originating from NiS nanoparticles. In the positive electrode, MWCNTs provide conduction pathways for the electrons to reach the current collector while NiS nanoparticles mainly initiate a faradaic reaction with electrolyte's ions.

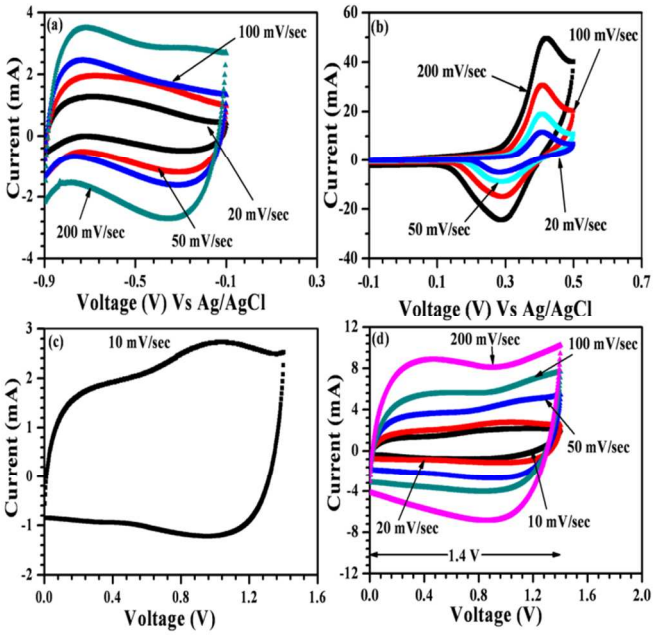

Fig. 6 Three electrode CV curves for (a) GNPs and (b) MWNS composite at various scan rates (activated carbon counter electrode, Ag/AgCl (sat. KCl) reference electrode); (c-d) CV curves for fabricated ASC at different scan rates in KOH (aq, 6mol dm^{-3}) electrolyte

A maximum specific capacitance of ~269 F g^{-1} at 20 mV s^{-1} was obtained for MWNS (m = 0.4 mg for MWNS) which is higher than that for GNPs. A specific capacitance of ~146 F g^{-1} was observed at a scan rate of 200 mV s^{-1}.

Journal of Materials Chemistry A Accepted Manuscript

At higher scan rates, the decrease in the specific capacitance is due to limited migration of the electrolyte ions into the electrode material. The optimal mass loading of each electrode for correct charge balance was determined using following relation:

$$m_+/m_- = \Delta V_- C_- / \Delta V_+ C_+$$

where C_- and C_+ are the capacitances (in F g^{-1}) measured at the same scan rate using the three electrode system for negative and positive electrodes, respectively and ΔV_+ and ΔV_- represents the working voltage window for the positive and negative electrodes, respectively. The desired ratio of masses for the positive and negative electrodes (m_+/m_-) was found to be ~0.72.

ASCs were fabricated using the calculated electrode masses (m_+/m_- = ~0.75) with a Whatman glass fibre paper separator and KOH (aq, 6 mol dm^{-3}) electrolyte. The ASCs were operated between 0 and 1.4 V. Typical CV curves are shown in Fig. 6(c-d). A quasi-rectangular-shaped CV curve was observed at 10 mV s^{-1} scan rate with small redox peaks due to the NiS nanoparticles. Similar shaped CV curves were observed at higher scan rates as shown in Fig. 6(d). At higher potentials, no rapid increase in the current was observed which indicates that water does not decompose into gases (O_2 and H_2 evolution).[30]

To understand further the electrochemical behaviour of ASCs, EIS was carried out in the frequency range 10 mHz to 100 kHz using an ac signal with 5 mV amplitude. A typical Nyquist plot (Re Z *vs* Im Z) for the fabricated ASCs is shown in Fig. 7. This ac impedance plot can be divided into two regions: one is the high frequency region, where the small semi-circle (see inset) indicates low resistance at the electrode/electrolyte interface; the second is the low frequency region, where the impedance plot becomes almost parallel to the vertical axis and indicates excellent capacitive behaviour.

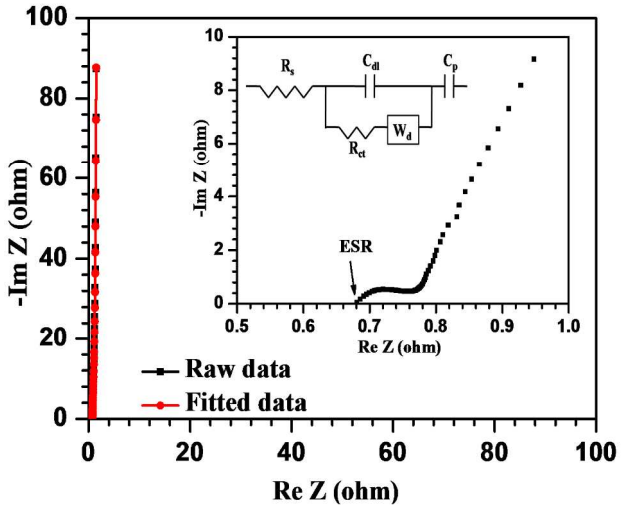

Fig. 7 Typical Nyquist plot (raw and fitted) for fabricated ASC. Inset shows the high frequency region and an equivalent circuit of this spectrum.

The equivalent series resistance (ESR) comprising of bulk electrolyte resistance, contact resistances and bulk electrode resistance, as estimated from x-intercept of the Nyquist plot, was found to be ~0.68 Ω. An equivalent circuit for the Nyquist plot is also given in the inset where R_s, R_{ct} are the series and charge transfer resistances, respectively and W_d is the Warburg resistance; C_{dl} and C_p are the double layer and pseudocapacitors, respectively.

Galvanostatic charge-discharge curves for the optimized ASCs were collected at different specific currents (1, 2, 3, 5, and 10 A g^{-1}) between 0 to 1.4 V as shown in Fig. 8(a). The specific capacitance was estimated from these curves using the following relation:

$$C_s = I.dt/(m.V)$$

where C_s represents the specific capacitance, I/m is the specific current (total mass m = 0.7 mg for both the electrodes), dt is the discharging time and V is the operating voltage window.

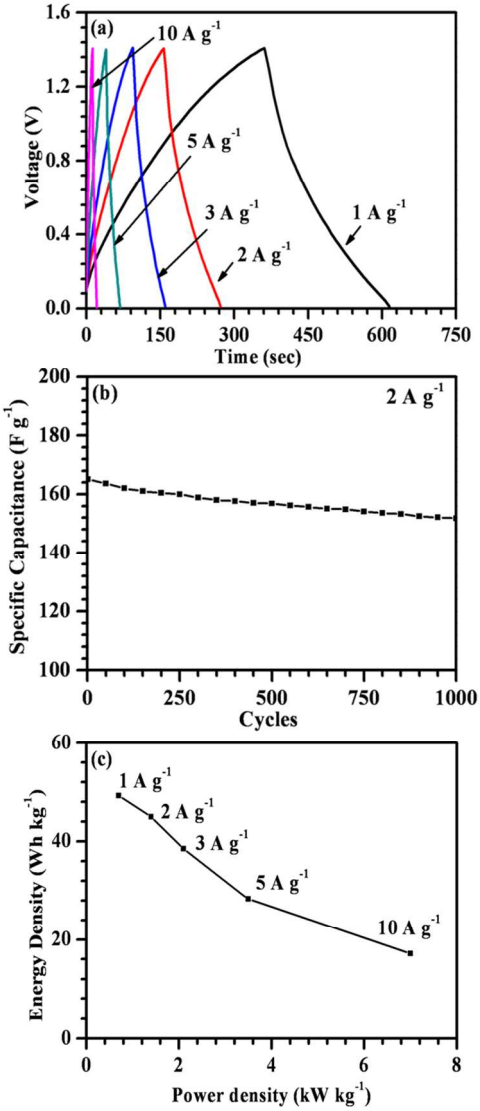

Fig. 8(a) galvanostatic charge-discharge curves at different specific currents (b) specific capacitance variation over 1000 charge-discharge cycles at 2 A g^{-1} (c) Ragone plot for ASC

At a specific current of 1 A g^{-1}, a specific capacitance of ~181 F g^{-1} was obtained. The specific capacitance values calculated at specific currents of 2, 3, 5 and 10 A g^{-1} were found to be ~165, 141, 104 and 63 F g^{-1}, respectively, indicating a good rate capability up to a specific current of 5 A g^{-1}. Fig. 8(b) shows

Journal of Materials Chemistry A Accepted Manuscript

This journal is © The Royal Society of Chemistry [year]

cycling behaviour at a current density of 2 A g^{-1}, with a retention of 92% even after 1000 cycles, illustrating good cyclic stability for practical application. In addition, impedance spectra was collected after 1000 charge-discharge operations and given in Fig. S6 (see ESI). An increase in the value of ESR is observed, which could be due to a slight expansion of the electrodes after cycling. The Ragone plot, highlighting overall performance of fabricated ASCs, is shown in Fig. 8(c). A maximum energy density of ~49 Wh kg^{-1} was achieved at 1 A g^{-1} specific current, which corresponds to a power density of 700 W kg^{-1}. At a higher specific current of 10 A g^{-1}, maximum power density of ~7 kW kg^{-1} was obtained whilst energy density reduced to ~17 Wh kg^{-1}. It must be mentioned that values quoted here for energy and power density are calculated by considering the mass of active materials only.

The aforementioned electrochemical features could be assigned to (a) a synergistic effect between MWCNTs structure and NiS nanoparticles in MWNS composite (b) a well developed large interfacial contact region at electrode/electrolyte interfaces. The performances of the ASCs reported here are superior when compared with previous reports on MWCNTs, NiS and other metal-sulphides-based composites in SCs.[18-20,31-34]

It should be noted that in previous studies the specific capacitance values were estimated using a three electrode system whereas, in this work, asymmetric two electrode cells were employed, giving more reliable/accurate device-related capacitance values. This report clearly reveals potential for metal-sulfide-decorated MWCNTs as electrodes in fabricating ASCs with excellent electrochemical performance.

4. Conclusion

In summary, the fabricated ASCs using MWNS and GNPs as positive and negative electrodes show good electrochemical performance. The ASC showed a maximum specific capacitance of ~181 F g^{-1} at a specific current of 1 A g^{-1} and good rate capability. In addition, ASC retains ~92% of initial capacitance after 1000 cycles, when cycled at 2 A g^{-1}. These electrochemical characteristics can be ascribed to high specific capacity and wide voltage window for the ASCs.

Acknowledgements

The authors acknowledge funding under the UK-India Education and Research Initiative (UKIERI) of the British Council, New Delhi, India. Arvinder Singh thanks the Council of Scientific and Industrial Research (CSIR) of India for the award of Junior Research Fellowship (JRF). Work in this area at the University of Surrey is also funded by Research Councils UK (EPSRC grant EP/H019596/1).

Notes and references

[1]*Department of Physics, Indian Institute of Technology Kharagpur, Kharagpur-721302, West Bengal, India.*

Fax: +91 (0)3222255303; Tel:+91(0)3222 283820;

[2]*Department of Chemistry, University of Surrey, Guildford, Surrey GU2 7XH, UK.*

Fax: +44 (0)1483683016; Tel:+44 (0)1483 686834

**E-mail: achandra@phy.iitkgp.ernet.in, a.roberts@surrey.ac.uk*

1 G. Wang, L. Zhang and J. Zhang,*Chem. Soc. Rev.*, 2012, 41, 797-828.
2 A.Chandra, A. J. Roberts, E. L. H. Yee and R. C. T. Slade, *Pure Appl. Chem.*, 2009, **81**, 1489-1498.
3 A.Chandra, A. J.Roberts and R.C.T. Slade, *Solid State Commun.*, 2008, **147**, 83-87.
4 L. L. Zhang and X. S. Zhao, *Chem. Soc. Rev.*, 2009, **38**, 2520-2531.
5 A. Singh and A. Chandra, *J. Appl. Electrochem.*, 2013, **43**, 773-782.
6 P. Simon and Y. Gogotsi, *Nat. Mater.*, 2008, **7**, 845-854.
7 X. Zhao, B. M. Sanchez, P. J. Dobson and P. S. Grant, *Nanoscale*, 2011, **3**, 839-855.
8 A. Balducci, U. Bardi, S. Caporali, M. Mastragostino and F. Soavi, *Electrochem. Commun.*, 2004, **6**, 566-570.
9 A. Lewandowski, A. Olejniczak, M. Galinski and I. Stepniak, *J. Power Sources*, 2010, **195**, 5814-5819.
10 F. Wang, S. Xiao, Y. Hou, C. Hu, L. Liu and Y. Wu, *RSC Adv.*, 2013, **3**, 13059-13084.
11 Z. Lei, J. Zhang and X. S. Zhao, *J. Mater. Chem.*, 2012, **22**, 153-160.
12 L. Demarconnay, E. Raymundo-Pinero and F. Beguin, *J. Power Sources*, 2011, **196**, 580-586.
13 C. Lai, M. Lu and L. Chen, *J. Mater. Chem.*, 2012, **22**, 19-30.
14 K. Aso, H. Kitaura, A. Hayashi and M. Tatsumisago, *J. Mater. Chem.*, 2011, **21**, 2987-2990.
15 S. Yang, H. Yao, M. Gao and S. Yu, *Cryst. Eng. Comm.*, 2009, **11**, 1383-1390.
16 H. Pan, J. Li and Y. P. Feng, *Nanoscale Res. Lett.*, 2010, **5**, 654-668.
17 B. Kim, H. Chung and W. Kim, *Nanotechnology*, 2012, **23**, 155401-155408.
18 A. Wang, H. Wang, S. Zhang, C. Mao, J. Song, H. Niu, B. Jin and Y. Tian, *Appl. Surf. Sci.*, 2013, **282**, 704-708.
19 B. T. Zhu, Z. Wang, S. Ding, J. S. Chen and X. W. Lou, *RSC Adv.*, 2011, **1**, 397-400.
20 Z. Xing, Q. Chu, X. Ren, J. Tian, A. M. Asiri, K. A. Alamry, A. O. A. Youbi and X. Sun, *Electrochem. Commun.*, 2013, **32**, 9-13.
21 F. Luan, G. Wang, Y. Ling, X. Lu, H. Wang, Y. Tong, X. X. Liu and Y. Li, *Nanoscale*, 2013, **5**, 7984-7990.
22 B. G. Choi, S. J. Chang, H. W. Kang, C. P. Park, H. J. Kim, W. H. Hong, S. G. Lee and Y. S. Huh, *Nanoscale*, 2012, **4**, 4983-4988.
23 D. C. Marcano, D. V. Kosynkin, J. M. Berlin, A. Sinitskii, Z. Sun, A. Slesarev, L. B. Alemany, W. Lu and J. M. Tour, *ACS Nano* , 2010, **4**, 4806-4814.
24 A. Singh and Amreesh Chandra, *phys. status solidi B*, 2013, **250**, 1483-1487.
25 D. L. Legrand, H. W. Nesbitt and G. M. Bancroft, *Am. Mineral.*, 1998, **83**, 1256-1265.
26 A. Ganguly, S. Sharma, P. Papakonstantinou and J. Hamilton, *J. Phys. Chem. C*, 2011, **115**, 17009-17019.
27 D. W. Bishop, P. S. Thomas and A. S. Ray, *Mater. Res. Bull.*, 1998, **33**, 1303-1306.
28 M. Yoshikawa, M. Murakami, K. Matsuda, T. Matsunobe, S. Sugie, K. Okada and H. Ishida, *J. Appl. Phys.*, 2005, **98**, 063531-063533.
29 M. Holtz, W. M. Duncan, S. Zollner and R. Liu, *J. Appl. Phys.*, 2000, **88**, 2523-2528.
30 D. Qu, *J. Appl. Electrochem.*, 2009, **39**, 867-871.
31 Z. Xing, Q. Chu, X. Ren, C. Ge, A. H. Qusti, A. M. Asiri, A. O. Al-Youbi and X. Sun, *J. Power Sources*, 2013, **245**, 463-467.
32 H. Zhang, X. Yu, D. Guo, B. Qu, M. Zhang, Q. Li and T. Wang, *ACS Appl. Mater. Interfaces*, 2013, **5**, 7335−7340.
33 S. W. Chou and J. Y. Lin,*J. Electrochem.Soc.*, 2013, **160**, D178-D182.
34 C. S. Dai, P. Y. Chien, J. Y. Lin, S. W. Chou, W. K. Wu, P. H. Li, K. Y.Wu and T. W.Lin, *ACS Appl. Mater. Interfaces*,2013, **5**, 12168−12174.

Journal of Materials Chemistry A Accepted Manuscript